2026 IEEE International Conference on Robotics and Automation (ICRA 2026)
June 1-5, 2026. Vienna, Austria

Simplified 3D control of magnetic objects by a triple-coil static unit on a robotic arm

Luca Cinus, Jessé Alves, Tamerlan Srymbetov, Marco Ferro,
Claudio Pacchierotti, Arianna Menciassi, Veronica Iacovacci

***Abstract*—Magnetic actuation is a powerful, non-contact method for controlling milli-scale robots. However existing mobile magnetic field sources face a difficult trade-off. Single-coil end-effectors are simple but underactuated, forcing complex and inefficient robot motions to steer objects. Conversely, multi-coil systems improve dexterity but introduce significant mechanical and control complexity. To cope with this challenge, we present a compact, fixed-configuration triple-coil electromagnetic end-effector mounted on a 7-DOF robotic arm. Our innovation lies in a hierarchical control strategy that decouples global and local actuation. A Control Lyapunov Function-based Quadratic Programming (QP-CLF) controller guides the robotic arm for large-scale repositioning, extending the workspace and minimizing required currents. Simultaneously, modulating the currents through the three coils provides fine, high-bandwidth electrical control over the local magnetic field and gradient. We validated this approach by steering 1, 2, and 3 mm magnetic spheres along complex spiral trajectories inside fluid-filled phantoms (water and oil). Our system was teleoperated under operator vision and demonstrated highly repeatable path passing performance, proving that this synergistic robot-electromagnet control provides a compelling balance of dexterity, compactness, and simplicity for advanced magnetic manipulation tasks.**

***Index Terms*—Micro/Nano robots, Motion Control, Optimization and optimal control**

I. Introduction

CONTROLLING micro- and milli-scale robots within constrained environments, such as the human vasculature or lab-on-a-chip devices, presents a major challenge for conventional robotics. Magnetic actuation offers a promising solution by enabling non-contact control [1], but existing systems face a critical trade-off between dexterity and complexity. Magnetic fields unique ability to penetrate tissue non-invasively [2] holds great promise for medical procedures in deep or delicate anatomical regions, but realizing this potential relies on overcoming significant control and hardware challenges.

When controlling a magnetic object, the first step is to choose how to generate fields and gradients in the workspace. Mobile permanent magnets, stationary arrays of electromagnets surrounding the workspace, and compact electromagnets that are themselves moved by a robot have been proposed so far to this purpose.

This work was supported by the European Commission under the Horizon Europe program (REGO Project, Grant #101070066).

Permanent magnets are widely used for their simplicity and ability to generate strong magnetic fields and gradients without electric power supply. In many applications the magnet is mounted on a robotic arm, which positions and orients it to shape the magnetic field in the workspace and steer the target object. This actuation approach has been employed in capsule endoscopy [3] [4], biopsy grippers [5], and magnetically guided catheters [6] [7], to mention a few potential applications. The field amplitude of a permanent magnet is fixed by its volume and grade, so fast modulation depends entirely on the robot motion. This reliance on mechanical reorientation forces the robotic arm into continuous, often large, movements to align the magnet axis with the desired force vector, increasing the risk of kinematic singularities and limiting maneuverability in constrained spaces.

Stationary electromagnets, in contrast, produce a tunable and real-time controllable magnetic field through regulated electric currents. This versatility makes them highly suitable for remote manipulation of untethered micro agents. Systems such as OctoMag [8], MiniMag [9] or BatMag [10] typically rely on large stationary coils positioned around the workspace, which are dimensioned to cope with field decay with the distance from the source. The substantial infrastructure, power, and cooling requirements of these large-scale systems hinder their clinical translation, motivating the development of more compact and mobile alternatives.

A more recent strategy aims to improve efficiency and reduce system footprint by bringing the electromagnetic source closer to the target, typically by mounting compact coils on a robotic manipulator. For example, DeltaMag [11] arranges three mobile coils on a parallel robotic structure to dynamically reconfigure the 3D magnetic field. More recently, a research group presented a four-coil system mounted on a 3-axis gantry to manipulate magnetic capsules in gastrointestinal applications [12]. Similarly, MagNeed [13] uses three needle-shaped coils to produce gradients of up to 3.5 T/m. The MILiMAC catheter [14] integrates three microcoils directly at its tip for endovascular navigation. On the other hand, single-coil systems are typically underactuated for arbitrary 3D field orientations. This lack of electrical dexterity forces the robotic manipulator to perform complex compensatory movements to reorient the field, which restricts the complexity of achievable trajectories for the target object. The use of multiple mobile

coils or even multiple robots can increase field tunability but introduces significant drawbacks, such as higher control complexity, mechanical burden, and overall bulkier setups. This creates a fundamental trade-off in mobile magnetic manipulation: single-coil systems [15] provide simpler designs but force the robot to perform all reorientation mechanically, while multi-coil systems [11], [13], [16] achieve electrical steering at the cost of significant mechanical and control complexity.

To address this trade-off, we propose a compact, fixed-configuration triple-coil electromagnetic end-effector mounted on a 7-DOF robotic arm (Figure 1), which simplifies both mechanics and control while providing full 3D magnetic actuation. This hybrid design results in decoupling the control problem: coarse, global positioning is handled by the robot, while fine, local magnetic field steering is achieved by current modulation. This synergy preserves full 3D manipulation capabilities for complex trajectories while significantly simplifying both the end-effector mechanical design and the control demand on the robot side.

The primary contributions of this paper are: (1) the design of a compact, fixed-configuration triple-coil end-effector that decouples local field steering from global positioning; (2) a hierarchical control framework combining a QP-CLF for optimal robot motion with model-based current profiles for local actuation; and (3) experimental validation demonstrating reliable open-loop steering of objects along complex 3D trajectories in viscous media.

To cope with these objectives, the paper is organized as follows. Section II introduces the wrist-mounted triple-coil module, describing both its geometry and associated electronics. Section III presents the electromagnetic model employed for coil design and control support. Section IV details the controller developed to guide the robotic arm through predefined poses while minimizing control effort. Section V describes the experimental protocol, and Section VI reports and discusses the obtained results.

II. System Overview

The overall setup of our considered system is represented in Figure 1: the proposed electromagnetic end-effector consists of three identical coils, mounted at the vertices of an equilateral triangle on a custom 3D-printed adapter, which is rigidly attached to the wrist of a 7-DOF Franka Emika Panda collaborative robot.

The three coils are powered by independent linear current drivers (NPS Z linear). These drivers are controlled by Arduino UNO, which receives high-level commands from a LabVIEW interface via USB. To generate the necessary analog voltage reference without a true digital-to-analog converter, we filter the Arduino PWM output through a low-pass RC filter (fc=1.59 Hz) to produce a smooth control signal.

With this hardware architecture the platform supports:

- **Global positioning:** The robotic arm repositions the triple-coil end-effector to follow a desired macro-trajectory. This strategy keeps the magnetic object within the coils optimal workspace, minimizing current consumption.
- **Local magnetic control:** the coil currents I_1, I_2, I_3 modulate the field $\mathbf{B}(\mathbf{x})$ and its gradient $\nabla\mathbf{B}(\mathbf{x})$ to generate forces/torques on a magnetic object.

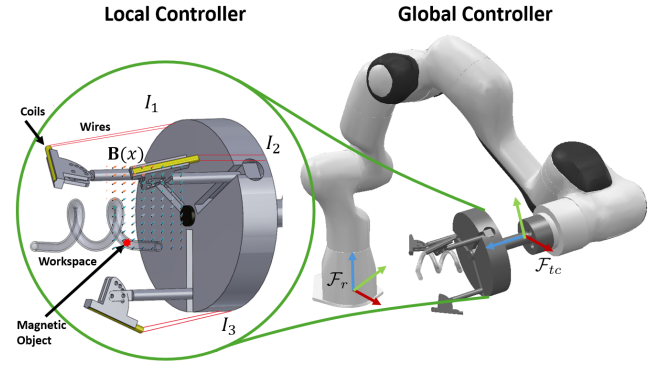

(a)

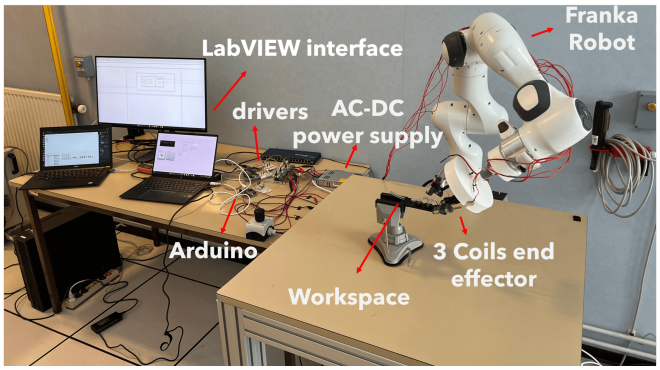

(b)

Fig. 1. **(a)** Schematization of the proposed triple-coil static unit on a robotics arm. A closeup of the triple-coil module highlights the arrangement of the three identical electromagnetic coils with its wires, on a 3D-printed wrist adapter. **(b)** Test setup that integrates the 7 DOF manipulator, the end-effector, the coils, power connections, and the electronic drivers. The coils are connected to independent current drivers controlled via an Arduino-based analog modulation scheme, which translates high-level commands from the LabVIEW interface into precise current profiles.

III. Numerical and Analytical Modeling

To enable real-time control, we developed a two-stage magnetic modeling approach. First, a high-fidelity Finite Element Method (FEM) simulation was carried out to accurately characterize the electromagnetic behavior of the coils. The resulting field data were then approximated through an analytical model based on linear superposition. Each coil k, with $k \in \{1, 2, 3\}$, was simulated in COMSOL Multiphysics® 6.2 using the Magnetic Fields module. The driving current I_k was varied in the range 0–5 A with a step of 0.5 A, where 5 A was considered as a safety upper limit for short-term excitation. From the obtained magnetic flux density $\mathbf{B}_k$, the corresponding field gradients and the forces acting on a magnetic object were subsequently derived. In particular,

the simulation results indicated that the magnetic flux density scales approximately linearly with the driving current, i.e., $\|\mathbf{B}_k\| \propto I_k$. Therefore, exploiting this linearity and following magnetostatic theory, we adopted a linear superposition model [17]:

$$\mathbf{B}(\mathbf{x}, \mathbf{I}) = \sum_{k=1}^{3} \mathbf{B}_k(\mathbf{x}) I_k, \tag{1}$$

where $\mathbf{x} \in \mathbb{R}^3$ denotes the spatial coordinates of the evaluation point in the workspace, $\mathbf{I} = [I_1, I_2, I_3]^\top$ are the coil currents and $\mathbf{B}(\mathbf{x}, \mathbf{I})$ is the magnetic field flux density.

The COMSOL simulations provided the magnetic field contributions $\mathbf{B}_k(\mathbf{x})$, which were exported on a uniform grid with 1 mm resolution over a $40 \times 40 \times 40$ mm^3 workspace. In MATLAB® R2024b, central finite differences were applied to compute the field gradients $\nabla \mathbf{B}_k(\mathbf{x})$. Based on the dipole approximation and on the superposition model (1), the magnetic force acting on a dipole with moment $\mathbf{m}$ is finally given by:

$$\mathbf{F}_{\text{mag}} = (\mathbf{m} \cdot \nabla)\mathbf{B}, \tag{2}$$

In all simulations and field maps, the magnetic moment $\mathbf{m}$ was assumed to be aligned with the local magnetic field $\mathbf{B}$ at each time instant, i.e., $\mathbf{m} \parallel \mathbf{B}$. Under this assumption, and with $\|\mathbf{m}\|$ treated as a constant (computed from the sphere volume and residual flux density), the force evaluation simplifies accordingly.

To validate the model, the magnetic flux density was measured at representative workspace locations for a single coil driven at 0.5 and 1.5 A using a Hall-effect sensor, and the results were compared against the model predictions. Measurements were performed on a 1 mm grid, within the sensitivity limits of the sensor. The relative error was computed as $\text{Error} = (X_{\text{measured}} - X_{\text{predicted}})/X_{\text{measured}} \times 100\%$, yielding a maximum absolute deviation below 20% (Figure 2). The observed discrepancy can be attributed to several factors, including uncertainties in sensor positioning relative to the coil and the limited sensitivity of the sensor. Nevertheless, since the magnetic fields employed in our experiments were relatively small, the deviations are considered acceptable within the context of the control task under investigation.

A. Coils dimensioning

The coils were dimensioned to guarantee that the magnetic field produced in any point of the selected $40 \times 40 \times 40$ mm^3 workspace never falls below 1 mT. This specification ensures sufficient actuation capabilities for milli-scale magnetic objects, while defining a workspace size that can be considered representative of biomedical applications.

With reference to Figure 1a, which highlights the reference frame $\mathcal{F}_{tc}$ attached to the triple-coil unit, coils are conceived to be mounted symmetrically at the vertices of an equilateral triangle with $\alpha = 120°$ separation, in order to maximize the in-plane isotropy of the generated magnetic field distribution.

Moreover, coils were also tilted with respect to the end-effector's main axis, to improve field penetration and

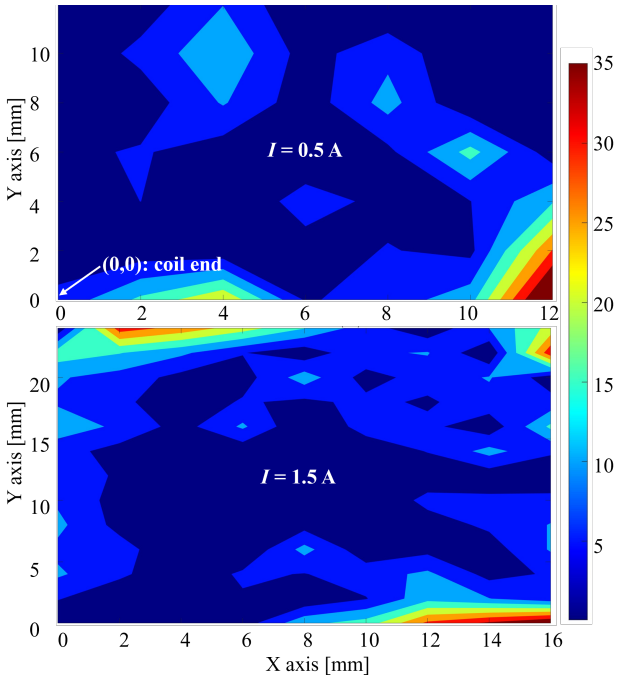

Fig. 2. Comparison between Hall-effect sensor measurements and FEM predictions of the magnetic flux density when a coil is driven at 0.5 and 1.5 A.

workspace homogeneity along the z direction (blue axis of $\mathcal{F}_{tc}$). To select the best tilt angle of the coil axis, for each candidate angle $\theta \in \{0°, 22.5°, 45°, 67.5°\}$, we evaluated field maps on xy-planes at different z heights and compared the resulting $\|\mathbf{B}\|$ distributions.

The mean field magnitude varied only slightly along the z-axis across different tilt angles θ, indicating limited sensitivity of the overall field strength to coil tilt. However, a component-wise analysis showed that tilting one coil closer to the z-axis ($\theta = 22.5°$) enhances the achievable z-projection of $\mathbf{B}$ (and the associated $\nabla\|\mathbf{B}\|$), thereby reducing the current required for vertical actuation. Based on these results, the final configuration employed two coils tilted at $\theta = 67.5°$ and one coil at $\theta = 22.5°$.

The two coils tilted at $\theta = 67.5°$ preserved strong lateral components for in-plane steering while maintaining a compact radial envelope, thereby reducing the risk of wrist collisions. The coil tilted at $\theta = 22.5°$ was instead optimized to generate stronger forward forces along the z-axis.

This design choice is consistent with previous studies on the number and placement of electromagnets: for 3D field control at a point, three independent coils are the minimal set of full rank [18], [19], while the position of electromagnets strongly affects isotropy and workspace for these kind of systems [20].

B. Path feasibility via Force balance

To relate our electromagnetic model to the motion of a magnetic object of moment $\mathbf{m}$, we modeled its interaction with the environment using a free-body diagram (Figure 3).

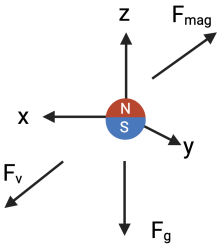

Fig. 3. Free-body diagram of a magnetized spherical object moving inside a viscous fluid under the influence of a magnetic field. The diagram illustrates the interactions between the magnetic force, the viscous drag force, and the buoyancy-corrected gravitational force

The forces considered are the following: the magnetic force $\mathbf{F}_{\text{mag}}$ (set by coil currents), the viscous drag $\mathbf{F}_v$ from the surrounding fluid, and the buoyancy-corrected weight $\mathbf{F}_g$. Along a planned path with maximum speed v, feasible motion requires the magnetic component to overcome environmental resistances,

$$\mathbf{F}_{\text{mag}} \;\geq\; (\mathbf{F}_v + \mathbf{F}_g), \tag{3}$$

For a sphere in low–Reynolds number (Stokes) flow,

$$\mathbf{F}_v = -\,6\pi\,\mu\,R\,\mathbf{v}, \tag{4}$$

$$\mathbf{F}_g = \big(\rho_s - \rho_f\big)\,V\,g\,\hat{\mathbf{g}}, \tag{5}$$

where μ is the fluid viscosity (Pa·s), R is the sphere radius (m), $\mathbf{v} \in \mathbb{R}^3$, with $\|\mathbf{v}\| \leq v$, is the sphere velocity relative to the fluid (m/s); ρ_s and ρ_f are the object and fluid densities (kg/m^3), respectively; $V = \frac{4}{3}\pi R^3$ is the sphere volume (m^3); $g \approx 9.81$ m/s^2 is gravitational acceleration; and $\hat{\mathbf{g}}$ is the unit vector along gravity (downward).

Under the common assumption that the magnetic moment aligns with the field ($\mathbf{m} \parallel \mathbf{B}$), the force equation simplifies to $\mathbf{F}_{\text{mag}} = \|\mathbf{m}\|\,\nabla\|\mathbf{B}\|$. The required gradient (and so current) depends on fluid viscosity μ, object volume V, speed v, as well as the object magnetization.

IV. Optimal Controller

A. Controller Overview

In our considered setup, the motion of the magnetic object is governed by a hierarchical control strategy combining two complementary modules: a global controller for the robotic manipulator and a local controller for the electromagnetic coils. At the global level, the manipulator actuates the three-coil frame $\mathcal{F}_{tc}$, whose pose is described by its position $\mathbf{p}_{\text{tc}}$ and orientation quaternion $\boldsymbol{\zeta}_{\text{tc}}$ with respect to the robot base frame $\mathcal{F}_r$. This global controller extends the effective workspace and enables tracking of long-range reference trajectories. The local controller provides fine positioning by actuating the electromagnetic coils directly through the currents I_1, I_2, I_3, ensuring precise motion within the immediate workspace of the three-coil unit. By modulating the magnetic field $\mathbf{B}(\mathbf{x})$ and its gradient $\nabla\mathbf{B}(\mathbf{x})$, the coils generate the magnetic force $\mathbf{F}_{\text{mag}}$ required for accurate positioning of the magnetic object. This dual actuation mechanism creates redundancy, since the object can be steered either by the local coil actuation or by the global motion of the manipulator, which can be exploited to optimize system performance (Figure 4).

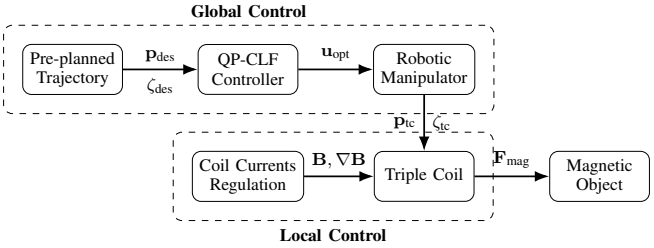

Fig. 4. Control architecture combining global and local controllers. The global controller moves the coil frame, while the local controller regulates magnetic currents for precise magnetic object actuation.

B. Global Controller Formulation

We define the state vector $\mathbf{x}$ as the joint positions of the 7-DOF manipulator, i.e., $\mathbf{x} = \mathbf{q} \in \mathbb{R}^7$. Therefore, the manipulator is modeled as a single-integrator system $\dot{\mathbf{x}} = \mathbf{u}$, where $\mathbf{u} \in \mathbb{R}^7$ are the joint velocities. The resulting model is linear and control-affine in the input, and therefore admits simple feedback solutions for pose regulation. However, in the considered setup, the design of the global controller must account for additional system-level requirements beyond pure pose tracking, in order to ensure continuous magnetic coupling between the triple-coil unit and the magnetic object. In particular, we require: (i) explicit enforcement of joint velocity limits to comply with actuator specifications; and (ii) avoidance of abrupt variations in joint velocities, as excessive accelerations of the triple-coil unit may disrupt the magnetic interaction and compromise the magnetic link during open-loop actuation.

To satisfy these requirements within a unified framework, we adopt a Quadratic Programming formulation with a Control Lyapunov Function (QP-CLF) constraint [21]. Compared to post-hoc saturation of classical Jacobian-based feedback controllers, the formulation guarantees asymptotic convergence of the end-effector pose, while the quadratic cost regulates control effort and penalizes successive input variations. Actuator bounds are incorporated directly as constraints, enabling simultaneous enforcement of stability, smoothness, and saturation limits that are critical for reliable magnetic actuation.

Therefore, the optimal control input is obtained as the solution of the following optimization problem:

$$\begin{aligned} \mathbf{u}_{\text{opt}} = \arg\min_{\mathbf{u}} \quad & \mathcal{C}(\mathbf{u}) \\ \text{s.t.} \quad & \mathbf{u}_{\text{lb}} \leq \mathbf{u} \leq \mathbf{u}_{\text{ub}}, \\ & \mathbf{a}_{\text{lb}} \leq A\mathbf{u} \leq \mathbf{a}_{\text{ub}}, \end{aligned} \tag{6}$$

where $\mathbf{u} \in \mathbb{R}^m$ is the control inputs and $\mathcal{C}(\mathbf{u})$ is the cost function. The matrix $A \in \mathbb{R}^{p\times m}$, with bounds $\mathbf{a}_{\text{lb}}, \mathbf{a}_{\text{ub}} \in \mathbb{R}^p$, denotes affine constraints that, along with the cost function, can encode specific control objectives. Finally, the bounds

$\mathbf{u}_{\text{lb}}, \mathbf{u}_{\text{ub}}$ impose actuator limits. In our case, the control objectives are:

*1) **Steer to the desired pose**:* Driving the triple-coil from its current pose $(\mathbf{p}_{\text{tc}}, \boldsymbol{\zeta}_{\text{tc}})$ to the desired pose $(\mathbf{p}_{\text{des}}, \boldsymbol{\zeta}_{\text{des}})$ requires regulating the system state to its reference, i.e., $\mathbf{x} \rightarrow \mathbf{x}_{\text{des}}$, where $(\mathbf{p}_{\text{tc}}, \boldsymbol{\zeta}_{\text{tc}}) = \text{FK}(\mathbf{x})$ denotes the forward kinematics of the robot manipulator, mapping the joint configuration to the pose of its end-effector (here, the triple-coil unit). To achieve this, we impose a Control Lyapunov Function (CLF) constraint as an affine constraint in the optimization problem (6). A CLF is a positive-definite, continuously differentiable function $V : \mathbb{R}^n \rightarrow \mathbb{R}$ that serves as a measure of the system's deviation from a desired state. By requiring its time derivative to satisfy an affine inequality in the control input $\mathbf{u}$ [21], such constraint guarantees that V decreases along the system trajectories, thereby ensuring asymptotic convergence. In this work, we defined the following Lyapunov function:

$$V(\mathbf{x}) = V_p(\mathbf{x}) + V_\zeta(\mathbf{x}), \tag{7}$$

where $V_p(\mathbf{x})$ enforces convergence of the triple-coil position, while $V_\zeta(\mathbf{x})$ accounts for the triple-coil orientation. The position Lyapunov candidate function is defined as $V_p(\mathbf{x}) = \frac{1}{2}\, \boldsymbol{e}_p^\top K_p \boldsymbol{e}_p$, where $K_p \in \mathbb{R}^{3\times3}$ is a positive definite gain matrix, and $\boldsymbol{e}_p = \mathbf{p}_{\text{des}} - \mathbf{p}_{\text{tc}}$ denotes the position error between the desired position $\mathbf{p}_{\text{des}} \in \mathbb{R}^3$ and the current triple-coil position $\mathbf{p}_{\text{tc}} \in \mathbb{R}^3$, obtained from the forward kinematic model of the robot.

Similarly, the orientation Lyapunov term is given by $V_\zeta(\mathbf{x}) = \frac{1}{2}\, \boldsymbol{e}_\zeta^\top K_\zeta \boldsymbol{e}_\zeta$, where $K_\zeta \in \mathbb{R}^{3\times3}$ is a positive definite gain matrix, and $\boldsymbol{e}_\zeta \in \mathbb{R}^3$ denotes the orientation error, computed from the difference between the desired unit quaternion $\zeta_{\text{des}} = [\eta_{\text{des}}; \boldsymbol{\epsilon}_{\text{des}}]$ and the current triple-coil unit quaternion $\zeta_{coil} = [\eta_{\text{tc}}; \boldsymbol{\epsilon}_{\text{tc}}]$:

$$\boldsymbol{e}_\zeta = -\eta_{\text{des}}\boldsymbol{\epsilon}_{\text{tc}} + \eta_{\text{tc}}\boldsymbol{\epsilon}_{\text{des}} - \boldsymbol{\epsilon}_{\text{des}} \times \boldsymbol{\epsilon}_{\text{tc}}. \tag{8}$$

*2) **Smooth Control Inputs**:* In addition, the QP formulation incorporates a cost function that regulates the control effort. In our case, two objectives are considered: (*i*) minimizing the magnitude of the control signal and (*ii*) penalizing variations between successive control inputs. The latter objective prevents abrupt changes in the commanded joint velocities, thus improving the smoothness and robustness of the actuation. We formalize this requirement by defining the following cost function:

$$C(\mathbf{u}) = \tfrac{1}{2}(\mathbf{u} - \mathbf{u}_{k-1})^\top H(\mathbf{u} - \mathbf{u}_{k-1}) = \tag{9}$$

$$= \tfrac{1}{2}\mathbf{u}^\top H\mathbf{u} + \mathbf{k}^\top\mathbf{u}, \tag{10}$$

where $H \succ 0$ is the weighting matrix, $\mathbf{u_k} \in \mathbb{R}^m$ is the current control input, and $\mathbf{u_{k-1}} \in \mathbb{R}^m$ is the control input from the previous time step. The expanded form (10) fits the standard QP structure with H as the quadratic term and $\mathbf{k} = -H\mathbf{u}_{k-1}$ as the linear term.

C. Local Controller Formulation

The local control strategy is formulated in open loop and relies on a temporal scheduling of coil actuation, synchronized with the global motion of the robotic manipulator. Since the position of the magnetic object within the workspace is not directly measurable, the magnetic object is assumed to remain near the center of the workspace of the triple-coil unit during locomotion. Under this assumption, and given the advancement trajectory $y(t)$ of the end-effector along the longitudinal axis (tracked by the global controller), a corresponding time profile of the magnetic force $\mathbf{F}_{\text{mag}}(t)$ is designed. This force profile, temporized with respect to $y(t)$, drives the sphere along the constrained path while the triple-coil unit is simultaneously advancing. Both the profile and its timing depend on the geometric characteristics of the workspace, such as its curvature and diameter.

From the dipole model described in Sec. III-B, the magnetic force exerted on the sphere can be expressed as a function of the coil currents. By inverting precomputed force values that map coil currents to field gradients, the coil currents $(I_1(t), I_2(t), I_3(t))$ required at each time instant to produce the desired $\mathbf{F}_{\text{mag}}(t)$ can be derived. This approach enables the generation of sufficient magnetic forces to overcome drag and buoyancy, thereby producing net forward locomotion of the sphere in synchrony with the global motion of the manipulator.

V. Experiments

We evaluate open-loop feasibility and repeatability on a challenging 3D spiral trajectory (Fig. 1a) that couples tight in-plane bends with continuous elevation changes to exercise full 3D steering. Trials were teleoperated under visual guidance of the user and span different media and sphere sizes.

We tested commercially available N42 permanent magnetic spheres of diameter $d \in \{1, 2, 3\}$ mm. Each sphere was tested in two fluid media with distinct viscosities: deionized water ($\mu \approx$1 mPa·s, $\rho \approx 1000$ kg/m^3) and silicone oil ($\mu \approx$50mPa·s, $\rho \approx 960$ kg/m^3). These parameters were varied to investigate the environmental interaction model of Sec. III-B and the capability of the controller to enable 3D motion of small-scale object featuring different magnetic dipoles.

Two customized workspaces were tested while varying the channel diameter and the distance between the coils and the workspace. Both of them contained a vessel-like path arranged in 3D to allow the object performing a spiral trajectory. The two workspaces differ by the channel size: the large workspace (LW) had inner diameter 5 mm and outer diameter 7 mm; the small workspace (SW) featured inner diameter 3.5 mm and outer diameter 6 mm. The path starting point was marked and the triple-coil module was positioned to match the planned start pose. The choice of testing two different workspace followed the force-balance considerations of Sec. III-B: smaller coil to object distance in SW, enabled by its reduced lumen, lowers the current needed to overcome drag and weight, whereas LW is appropriate for larger spheres. As a consequence, d=3 mm is tested in the

large workspace, d=2 mm in both workspaces, and d=1 mm in the small workspace.

Tests were conducted in *open loop* with respect to the magnetic object. A desired Cartesian trajectory $(\mathbf{p}_{\mathrm{des}}(t),\, \boldsymbol{\zeta}_{\mathrm{des}}(t))$ for the pose of the triple-coil unit, represented with the frame $\mathcal{F}_{tc}$, was provided and tracked by the global controller. This trajectory was generated offline by interpolating keyframes along the tube centerline in a simulation environment, to obtain a smooth path. The resulting reference was defined as $\mathbf{p}_{\mathrm{des}}(t) = [x_0,\ y(t),\ z_0]^\top$ and $\boldsymbol{\zeta}_{\mathrm{des}}(t) = \boldsymbol{\zeta}_0$, with $x_0 = 0.56$ m, $z_0 = 0.34$ m, and fixed orientation quaternion $\boldsymbol{\zeta}_0 = [0.42,\ 0.53,\ -0.56,\ 0.47]$. The y-coordinate followed a linear trajectory over a time interval $T = 36$ s, namely

$$y(t) = y_0 + \tfrac{t}{T}(y_{\mathrm{end}} - y_0), \tag{11}$$

with $t \in [0, T]$, $y_0 = 0.22$ m and $y_{\mathrm{end}} = 0.30$ m.

The QP–CLF controller (Sec. IV) tracked this trajectory by generating joint velocity commands $\mathbf{u} = \dot{\mathbf{q}}$ for the 7-DOF arm, while the three coil currents follow precomputed profiles $I_k(t)$ derived offline from the model and the force-balance requirement of Sec. III-B. The controller was tuned to guarantee smooth and stable motion of the triple-coil system during experiments. In our formulation, the gamma function was defined as $\gamma(V(x)) = k_\gamma V(x)$, where k_γ is a positive gain. Furthermore, the joint velocity bounds were set according to the Franka Emika Panda specifications . All the controller gains used in this work are reported in Table I. Timing between robot trajectory and coil currents was adjusted so that $\mathbf{q}(t)$ and $I_k(t)$ were synchronized to steer the sphere in a controllable fashion without online corrections. For each medium and sphere size we perform $n = 10$ independent repetitions. Before each trial, the sphere was manually returned to the marked start location using tweezers, ensuring a consistent starting point for each repetition. A trial was stopped either when the sphere entered the goal region (success) or the sphere was determined stalled (defined as making no discernible forward progress for 5 consecutive seconds), at which point the trial was marked as a failure. The primary outcome obtained in these tests was the *success rate* $\mathrm{SR} = \frac{\#\mathrm{success}}{\#\mathrm{trials}}$, defined as the fraction of trials in which the sphere reached the goal region.

TABLE I
QP-CLF PARAMETERS

Parameter	Value
Gamma function gain k_γ	1.0
Position gain K_p	$10 \times \mathbb{I}_{3\times3}$
Orientation gain K_ζ	$6 \times \mathbb{I}_{3\times3}$
Quadratic Cost Matrix H	$\mathbb{I}_{7\times7}$

TABLE II
PARAMETERS SUMMARY

Parameter	Value
Coil length L_1	50 mm
Core diameter D	5 mm (soft iron, $\mu_r \approx 4000$)
Wire diameter d_{Cu}	0.3 mm
Layers n_ℓ	5 (radial build $\approx n_\ell d_{\mathrm{Cu}} = 1.5$ mm)
Turns N	≈ 830
Outer diameter D_{out}	$D + 2n_\ell d_{\mathrm{Cu}} \approx 8$ mm
Current range I	0–5 A
Azimuthal spacing	120° between coil axes
Tilt angle θ	67.5°, 67.5° and 22.5° wrt tool z-axis

VI. Results and Discussions

A. Coils dimensioning

The coil geometry was selected from the modeling of (Sec. III-A) to cope with the force balance analysis that specifies the minimum field magnitude gradient needed to move the magnetic object. Each coil consists of a soft-iron core of 5 mm diameter and 50 mm in length, wound with copper wire of 0.3 mm in diameter (Table II). A maximum of five layers were implemented, corresponding to approximately 830 turns.

The choice of five layers provided a trade-off between sufficient turns to reach the target field levels in the workspace, while keeping bulkiness and heating within limits. Indeed, fewer layers were predicted to reduce field strength below the target in the central workspace, whereas additional layers would increase resistance, thermal load and bulkiness of the system.

The three coils were mounted on a 3D printed wrist adapter. Their bases lie at the vertices of an equilateral triangle of side 40 mm, whose centroid is aligned with the tool z-axis. The field performance was assessed in simulation: the magnetic flux density at the coil tip reaches 130 mT at 5 A, while the coil geometry was sized so that the field magnitude remained above $\sim$1 mT throughout the $40 \times 40 \times 40$ mm^3 workspace (Sec.III-A), providing sufficient force for milli-scale actuation.

B. Experimental validation

This subsection reports the experiments on the chosen path and interprets the outcomes through the environmental force-balance model introduced earlier. The robotic arm executes a slow, continuous global repositioning (at an average end-effector speed of $\approx$ 2.3 mm/s) to keep the region of strongest gradient aligned with the tube centerline, while local magnetic control relies on a timed, sequential activation of the three coils. Each coil is driven with the same current amplitude for an equal time window Δt and each coil is activated sequentially for the same time interval. This cycle provides a smooth reorientation of the field direction across the spiral valleys, allowing the sphere to progress along the path without continuous wrist reorientation Figure 5. Table III summarizes the open-loop tests outcome across media, workspaces, and sphere sizes. In five out of eight conditions the success rate is $\mathrm{SR} = 1.00$, with the remaining cases achieving $\mathrm{SR} = 0.90$ (SW–H_2O, $d = 1$ mm) and $\mathrm{SR} = 0.80$ (LW–H_2O, $d = 2$ mm; SW–Oil, $d = 1$ mm).

Across workspaces and sphere sizes, oil consistently requires higher minimum peak currents and typically longer activation windows than water, as expected from its higher

TABLE III

OPEN-LOOP EXPERIMENTS OUTCOME BY CONDITION. $\min|I_k|$ IS THE MINIMUM PEAK COIL CURRENT REQUIRED FOR SUCCESS, AND Δt IS THE ACTIVATION TIME FOR EACH COIL IN THE SEQUENCE.

Workspace	Medium	d [mm]	SR	$\min\|I_k\|$ [A]	Δt [s]
Large workspace					
LW	H_2O	2	0.80	2.2	1.5
LW	H_2O	3	1.00	1.6	1.5
LW	Oil	2	1.00	2.8	3.5
LW	Oil	3	1.00	2.1	3.5
Small workspace					
SW	H_2O	1	0.90	1.1	1.0
SW	H_2O	2	1.00	0.7	1.0
SW	Oil	1	0.80	1.4	1.5
SW	Oil	2	1.00	1.0	1.5

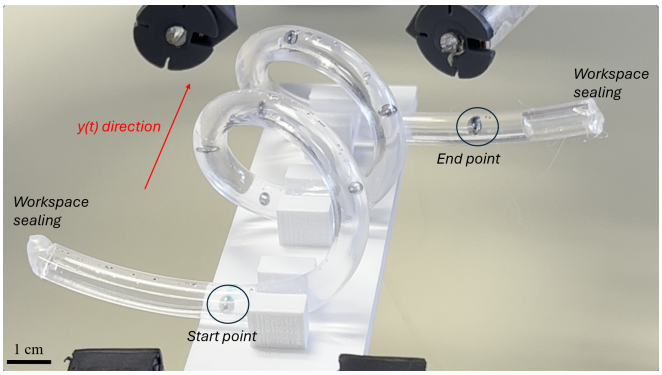

Fig. 5. Sequential video frames extracted from experimental trials (H_2O, LW, $d = 3$ mm), demonstrating the ability of the triple-coil robotic system to steer a magnetic sphere along a spiral-shaped path inside a confined tube. The images capture the progressive displacement of the object under global repositioning of the robot and timed local activation of the coils.

viscosity and drag. This trend matches the force-balance prediction that larger hydrodynamic resistances must be compensated by stronger magnetic forces.

To highlight the effect of coil-object distance, we compare the same sphere size and medium across workspaces. The SW systematically reduces current demand and activation time: for $d = 2$ mm in water, SW achieves $\mathrm{SR} = 1.00$ with $\min|I_k| = 0.7$ A and $\Delta t = 1.0$ s, whereas LW needs 2.2 A and 1.5 s and achieves $\mathrm{SR} = 0.80$; in oil, SW succeeds with 1.0 A and 1.5 s (SR$=1.00$) versus LW requiring 2.8 A and 3.5 s (SR$=1.00$). Smaller standoff strengthens the local gradient at the object, lowering peak currents and activation times and improving robustness, especially in water.

Sphere size is another critical parameter: larger spheres provide higher magnetic moment ($\|\mathbf{m}\| \propto V$) and therefore require smaller currents to reach the target at a given gradient. Overall, increasing d improves success and reduces current, provided the sphere and lumen remain compatible.

Regarding the controller performance, we evaluate the proposed QP-CLF formulation by analyzing the tracking error between the desired and actual poses of the triple-coil system.

The results are quantified using the Root Mean Square

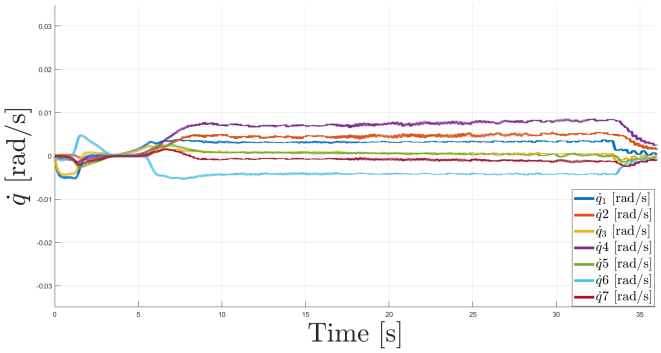

Fig. 6. Joint velocity control signals generated by the QP-CLF controller.

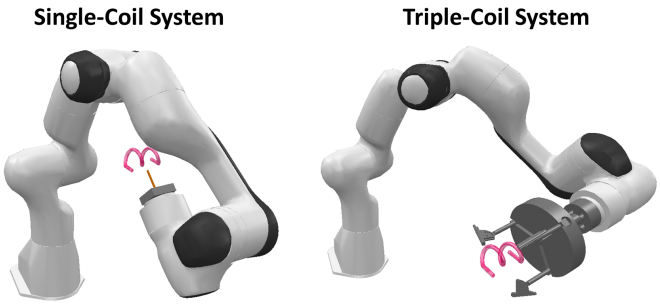

Fig. 7. Comparative simulation of a single-coil and triple-coil system along the same trajectory using CoppeliaSim.

Error (RMSE), yielding an RMSE of 2.26 mm for position, which corresponds to less than 3% of the total 80 mm path length, and 0.123° for orientation.

The corresponding control signals, i.e., the joint velocities of the robotic manipulator, are shown in Figure 6. These results highlight the main advantages of the QP-CLF formulation over other simple and well-established feedback solutions. First, actuator constraints are handled by enforcing saturation limits on the joint velocities, ensuring safe operation within the robot's specifications. Second, by minimizing both the magnitude of the joint velocities and their variation across steps, the controller produces smooth and stable motion, preventing excessive coil accelerations that could compromise the magnetic link. Finally, the framework provides a principled basis for extending the controller to more complex manipulation tasks. Additional objectives or constraints can be incorporated directly into the optimization problem without modifying the stability mechanism. For example, integrating Control Barrier Functions (CBFs) would enable safety-critical constraints such as obstacle avoidance, dexterity preservation near singularities, or sensing-aware motion strategies, as we preliminary investigated on different electromagnetic systems [22], [23]. This modular structure facilitates the transition from the present open-loop validation toward constrained, feedback-driven magnetic manipulation in realistic scenarios.

In addition, the proposed design also contributes to preserving robustness against manipulator singularities. Indeed, in a

hypothetical single-coil configuration, the robot wrist must continuously reorient to align the coil axis with the desired magnetic force direction, which can drive the manipulator toward unfavorable kinematic configurations. In contrast, the triple-coil architecture allows electrical reorientation of the magnetic field while maintaining a more neutral wrist pose.

To illustrate this structural advantage, we qualitatively compared the manipulator configurations along the planned trajectory for two scenarios: a single-coil end-effector and the proposed triple-coil unit. Figure 7 shows that, in the single-coil case, the wrist approaches near-singular configurations in the tightest curves, corresponding to alignment of joints 4 and 6 and a consequent loss of rotational dexterity. The triple-coil configuration, instead, maintains feasible joint postures throughout the motion, thereby reducing proximity to singularities while preserving the desired trajectory.

VII. Conclusion

This work addresses a key trade-off between dexterity and complexity in mobile magnetic manipulation. We introduced a compact, fixed-configuration triple-coil end-effector on a 7-DOF robotic arm that synergistically decouples global and local control. A QP-CLF controller ensured that the robotic arm executes smooth, large-scale motions that are robust to kinematic singularities, while local current modulation provided fine, electrical steering of the magnetic object. Our open-loop experimental validation demonstrated the system effectiveness and the predictive power of our physical model. We achieved reliable steering of magnetic spheres along challenging 3D spiral paths, with success rates reaching 100% in five out of eight conditions and precise end-effector tracking (2.26 mm RMSE in position and 0.123° in orientation). This approach successfully balances hardware simplicity with 3D manipulation capability, offering a good alternative to under-actuated single-coil systems and mechanically complex multi-coil platforms. Future work will focus on incorporating closed-loop visual feedback to increase robustness and precision, as well as integrating advanced techniques like CBFs to enable autonomous navigation in constrained environments.

References

[1] V. Iacovacci, E. Diller, D. Ahmed, and A. Menciassi, "Medical microrobots," *Annual Review of Biomedical Engineering*, vol. 26, pp. 561–591, 2024, first published online: April 9, 2024. [Online]. Available: https://doi.org/10.1146/annurev-bioeng-081523-033131

[2] J. Lin, Q. Cong, and D. Zhang, "Magnetic microrobots for in vivo cargo delivery: A review," *Micromachines*, vol. 15, no. 5, 2024. [Online]. Available: https://www.mdpi.com/2072-666X/15/5/664

[3] A. W. Mahoney and J. J. Abbott, "Five-degree-of-freedom manipulation of an untethered magnetic device in fluid using a single permanent magnet with application in stomach capsule endoscopy," *The International Journal of Robotics Research*, vol. 35, no. 1–3, pp. 129–147, 2015.

[4] G. Pittiglio, L. Barducci, J. W. Martin, J. C. Norton, C. A. Avizzano, K. L. Obstein, and P. Valdastri, "Magnetic levitation for soft-tethered capsule colonoscopy actuated with a single permanent magnet: A dynamic control approach," *IEEE Robotics and Automation Letters*, vol. 4, no. 2, pp. 1224–1231, 2019.

[5] Q. Jin, Y. Yang, J. A. Jackson, C. Yoon, and D. H. Gracias, "Untethered single cell grippers for active biopsy," *Nano Letters*, vol. 20, no. 7, pp. 5383–5390, 2020.

[6] C. Chautems, S. Lyttle, Q. Boehler, and B. Nelson, "Design and evaluation of a steerable magnetic sheath for cardiac ablations," *IEEE Robotics and Automation Letters*, vol. PP, pp. 1–1, 07 2018.

[7] L. Brockdorff, C. M. Heunis, J. Sikorski, and S. Misra, "Hybrid trajectory planning of two permanent magnets for medical robotic applications," in *2024 IEEE International Conference on Robotics and Automation (ICRA)*. IEEE, 2024, p. to appear.

[8] M. P. Kummer, J. J. Abbott, B. E. Kratochvil, R. Borer, A. Sengul, and B. J. Nelson, "Octomag: An electromagnetic system for 5-dof wireless micromanipulation," *IEEE Transactions on Robotics*, vol. 26, no. 6, pp. 1006–1017, 2010.

[9] B. E. Kratochvil, M. P. Kummer, S. Erni, R. Borer, D. R. Frutiger, S. Schürle, and B. J. Nelson, "Minimag: A hemispherical electromagnetic system for 5-dof wireless micromanipulation," in *Experimental Robotics*, ser. Springer Tracts in Advanced Robotics. Springer Berlin Heidelberg, 2014, vol. 79, pp. 317–329.

[10] F. Ongaro, S. Pane, S. Scheggi, and S. Misra, "Design of an electromagnetic setup for independent three-dimensional control of pairs of identical and nonidentical microrobots," *IEEE Transactions on Robotics*, vol. 35, no. 1, pp. 174–183, 2019.

[11] L. Yang, X. Du, E. Yu, D. Jin, and L. Zhang, "Deltamag: An electromagnetic manipulation system with parallel mobile coils," in *2019 International Conference on Robotics and Automation (ICRA)*, 2019, pp. 9814–9820.

[12] X. Li, D. Zeng, H. Xu, Q. Zhang, and B. Liao, "Magnetic actuation for wireless capsule endoscopy in a large workspace using a mobile-coil system," *Micromachines*, vol. 15, no. 11, 2024. [Online]. Available: https://www.mdpi.com/2072-666X/15/11/1373

[13] C. M. Heunis, Y. P. Wotte, J. Sikorski, G. P. Furtado, and S. Misra, "Magneed: Needle-shaped electromagnets for localized actuation within compact workspaces," *IEEE Robotics and Automation Letters*, vol. 7, no. 4, pp. 8973–8980, 2022.

[14] J. Sikorski, S. Mohanty, and S. Misra, "Milimac: Flexible catheter with miniaturized electromagnets as a small-footprint system for microrobotic tasks," *IEEE Robotics and Automation Letters*, vol. 5, no. 4, pp. 5260–5267, 2020.

[15] C. M. Heunis, Y. P. Wotte, J. Sikorski, G. P. Furtado, and S. Misra, "The armm system - autonomous steering of magnetically-actuated catheters: Towards endovascular applications," *IEEE Robotics and Automation Letters*, vol. 5, no. 2, pp. 705–712, 2020.

[16] N. O. Osinde, M. Etiévant, J. B. Byiringiro, and N. Andreff, "Calibration of a multi-mobile coil magnetic manipulation system utilizing a control-oriented magnetic model," *Mechatronics*, vol. 84, p. 102774, 2022. [Online]. Available: https://doi.org/10.1016/j.mechatronics.2022.102774

[17] S. L. Charreyron, Q. Boehler, B. Kim, C. Weibel, C. Chautems, and B. J. Nelson, "Modeling electromagnetic navigation systems," *IEEE Transactions on Robotics*, vol. 37, no. 4, pp. 1009–1021, Aug. 2021.

[18] A. J. Petruska and B. J. Nelson, "Minimum bounds on the number of electromagnets required for remote magnetic manipulation," *IEEE Transactions on Robotics*, vol. 31, no. 3, pp. 714–722, 2015.

[19] M. Cai, Z. Qi, Y. Cao, X. Wu, T. Xu, and L. Zhang, "Magnetic field-priority force control for automated manipulation in large workspaces with reconfigurable electromagnetic actuation system," *IEEE Transactions on Industrial Electronics*, vol. 72, no. 2, pp. 1732–1742, Feb 2025. [Online]. Available: https://doi.org/10.1109/TIE.2024.3426055

[20] A. Pourkand and J. J. Abbott, "A critical analysis of eight-electromagnet manipulation systems: The role of electromagnet configuration on strength, isotropy, and access," *IEEE Robotics and Automation Letters*, vol. 3, no. 3, pp. 2957–2962, 2018.

[21] A. D. Ames, S. Coogan, M. Egerstedt, G. Notomista, K. Sreenath, and P. Tabuada, "Control barrier functions: Theory and applications," in *2019 18th European control conference (ECC)*. Ieee, 2019, pp. 3420–3431.

[22] M. Ferro, F. N. Piñan Basualdo, P. R. Giordano, S. Misra, and C. Pacchierotti, "Experimental evaluation of haptic shared control for multiple electromagnetic untethered microrobots," *IEEE Transactions on Automation Science and Engineering*, vol. 22, pp. 8069–8080, 2025.

[23] L. Raphalen, M. Ferro, N. R. Posselli, P. R. Giordano, S. Misra, and C. Pacchierotti, "Constrained optimization for safe and visibility-aware shared control of magnetically actuated microrobots," *IEEE Transactions on Automation Science and Engineering*, 2026.